Permeation and dynamics of an open-activated TRPV1 channel

(Article begins on next page)

10 April 2024

Accepted Manuscript

Permeation and dynamics of an open-activated TrpV1 channel

Leonardo Darre, Simone Furini, Carmen Domene

Please cite this article as: Darre, L., Furini, S. & Domene, C., Permeation and dynamics of an open-activated TrpV1 channel, *Journal of Molecular Biology* (2014), doi: 10.1016/j.jmb.2014.11.016

Permeation and dynamics of an open-activated TrpV1 channel

Leonardo Darre[a], Simone Furini[b], and Carmen Domene[a,c,1]

[a]Department of Chemistry, King's College London, Britannia House, 7 Trinity Street, London SE1 1DB, UK

[b]Department of Medical Biotechnologies, University of Siena, viale Mario Bracci 16, I-53100, Siena, Italy

[c]Chemistry Research Laboratory, Mansfield Road, University of Oxford, Oxford OX1 3TA, UK

[1]Corresponding author: carmen.domene@kcl.ac.uk

Tel: +44 - (0) 2078483868

Abstract

Transient receptor potential (TRP) ion channels constitute a large and diverse protein family, found in yeast and widespread in the animal kingdom. TRP channels work as sensors for a wide range of cellular and environmental signals. Understanding how these channels respond to physical and chemical stimuli has been hindered by the limited structural information available until now. The three-dimensional structure of the vanilloid receptor 1 (TRPV1) was recently determined by single particle electron cryo-microscopy, offering for the first time the opportunity to explore ionic conduction in TRP channels at atomic detail. In this study, we present molecular dynamics simulations of the open-activated pore-domain of TRPV1 in the presence of three cationic species: Na^+, Ca^{2+} and K^+. The dynamics of these ions while interacting with the channel pore allowed us to rationalize their permeation mechanism in terms of a pathway involving three binding sites at the intracellular cavity, and the extracellular and intracellular entrance of the selectivity filter. Furthermore, conformational analysis of the pore in the presence of these ions reveals specific ion-mediated structural changes in the selectivity filter, which influences the permeability properties of the TRPV1 channel.

Introduction

Transient receptor potential (TRP) channels constitute a superfamily of cation channels characterized by their remarkable diversity in ionic selectivity and activation mechanisms, responding to a wide range of chemical and physical stimuli [1]. They participate in a plethora of functions in excitable and non-excitable cells playing a critical role in sensory physiology. Furthermore, they act both at the cell (synaptic activity and secretion of hormones) and organismic (touch, hearing, taste, olfaction, vision and thermal sensation) levels in animals ranging from worms to humans [1]. Such widespread physiological activity translates into a tremendous potential for TRP-associated channelopathies. In fact, several hereditary diseases caused by defects in TRP genes have been described (i.e. Charcot-Marie-Tooth type 2C, stationary night blindness, lateral sclerosis/parkinsonism dementia complex, familial heart block type I, polycystic kidney disease) [2]. Accordingly, TRP channels constitute a major pharmacological target, and the elucidation of the mechanisms underlying their response to physiological stimuli or drugs is key for notable advances in human disease treatment. Advances in such direction have been limited by the lack of experimental structural data. This barrier has been recently overpassed by the determination of the three-dimensional structure of the vanilloid receptor 1 (TRPV1) by means of single particle electron cryo-microscopy [3].

TRPV1 is the main representative of a subfamily of thermosensitive TRP channels that enable somatosensory cells to detect temperature changes in the environment, being activated by pernicious high temperatures. Additionally, tissue damage and inflammation products modulate the channel by decreasing its thermal activation threshold (~43ºC). This feature makes the TRPV1 channel an essential player in the molecular mechanisms responsible for injury-related hyperalgesia and pain hypersensitivity (see [4] and references therein). A daily example of its physiological function comes from its activity as receptor of capsaicin, the molecule responsible for the burning pain induced by chili peppers [5].

As previously suggested for the family of TRP channels [6], the TRPV1 structure revealed an overall trans-membrane tetrameric topology that resembles that of voltage-gated channels, and exhibits a four-fold symmetry arrangement of the subunits around a central ion pore. Each subunit consists of six trans-membrane α-helices (S1–S6) plus a re-entrant loop-helix domain located between S5 and S6, which adopt a cone shaped arrangement that forms the selectivity filter (SF). Segments S5, S6 and the SF domain constitute the central pore of the channel, which is flanked by a voltage-sensor-like domain formed by the S1-S4 segments [3]. The structure also provides details of TRP-specific domains: (i) four ankyrin repeats at the N terminus, reported to be responsible for multiple ligand binding and modulation of the channel sensitivity [7], (ii) the P360–V415 linker, conserved among TRPV subtypes, and which connects the ankyrin repeats to the S1 helix, and (iii) an extended and kinked interfacial helix following S6, which corresponds to the signature 'TRP domain' found in many TRP channels [1].

Permeability of different ions through TRPV1 was assessed by Caterina et al. [5] who described a preference of

3

TRPV1 for divalent species (Ca^{2+} and Mg^{2+}) over monovalent ions (Na^+, K^+ and Cs^+) with negligible differences among these. More recently, a 'dynamic selectivity' view has been proposed where the permeability to different cationic species varies in a time- and agonist concentration-dependent manner [8]. In this model, such selectivity changes would be accompanied by structural rearrangements at the SF. From a mechanistic point of view, the wider diameter of the pore compared to the diameter of the cations argues against a sieving phenomenon. One characteristic of TRPV channels worth noting is the presence of negatively charged residues in the outer region of the SF, which could act as a basin for cation attraction. In fact, in the case of the highly Ca^{2+} selective TRPV6 channel, the ionic selectivity is achieved by high affinity binding to carboxylate groups at the SF [9]. A similar scenario, involving residue D646, has been proposed to explain Ca^{2+} selectivity in TRPV1.

In the present work, by means of molecular dynamics simulations and the recently published structure of the TRPV1 channel in the open-activated conformation (Protein Data Bank entry 3J5Q) the aim is to build up on our knowledge of permeation properties of ion channels [10–21]. In order to gain atomistic insight into the cationic specific permeation phenomena, three ionic solutions were considered: NaCl, KCl and $CaCl_2$.

Results

Molecular Dynamics (MD) simulations of the pore-domain of the TRPV1 channel inserted in a model lipid bilayer have been carried in the presence of 150 mM of NaCl, KCl and $CaCl_2$. Two independent MD trajectories were simulated for each ion configuration, for a cumulative simulation time of 1.6 μs. Compared to the experimental structure, the simulated protein lacks helices S1-S4 and the intracellular domain of the channel. Neglecting the voltage sensor and the intracellular domain was shown to destabilize the open state of the intracellular gate in other ion channels [22]. Therefore, as we would like to study conduction events, closure of the intracellular gate was prevented by applying weak harmonic potentials that restrained the Cα atoms of the inner and outer helices to their experimental positions (see Methods section). These restraints are not expected to affect the permeation properties of the channel on the time scales considered in this study. In addition, the experimental structure of the open-activated state of TRPV1 included the vanilloid agonist resiniferatoxin (RTX) and the vanillotoxin DkTx, both absent in the simulation models. RTX causes the opening of the intracellular gate, as evidenced by a comparison with the apo structure of TRPV1. Since the intracellular gate was harmonically restrained to the open-state during the simulations, the absence of RTX is unlikely to modify the results. DkTX was used in the experiments to trap the channel in the open-activated state, preventing the frequent transitions of the channel toward the inactivated state [23]. Channel inactivation is a slow process compared to the time-scale of the MD simulations presented in this study. Therefore, the absence of DkTX will not affect the conformational state of the protein, and in addition, it allows us to sample the dynamics of the SF in a relevant physiological state.

The root mean square deviation (RMSD) of the protein backbone atoms stabilized in a few nanoseconds, and all the

secondary structural elements observed in the experimental structure were preserved during the MD trajectories (Figure S1 in Supplementary Material). Two regions with high affinity for cations were observed along the pore of TRPV1; they correspond to the intracellular cavity and the SF respectively (Figure 1). The region in the channel cavity with high affinity for cations, denoted SC, extends from residues I679 at the intracellular side, to residues Y671 at the extracellular side. In the presence of K^+ or Na^+ ions, SC switches between an empty state and single occupancy (75% and 61% of the time for Na^+ and K^+ respectively). In contrast, SC is always occupied by an ion which entered the cavity during the equilibration process in the simulations with Ca^{2+} ions. The cation-binding region at the inner entrance of the SF, denoted SF1, is centered at the carbonyl oxygen atoms of residues G643, while at the outer entrance of the permeation pathway, the SF is lined by eight negatively charged residues (D646 and E648). This excess of negative charge density defines a highly attractive region for cations, denoted SF2. In simulations with Na^+ ions, SF1 was found empty or occupied by one ion most of the time (respectively 51% and 47%), while SF2 was occupied by two, three, or four ions with simulation time percentages of 22%, 42%, and 30%, respectively. In the presence of K^+ ions, the most likely configurations were with SF1 empty (20%) or occupied by a single ion (72%), and SF2 doubly (38%) or triple (39%) occupied by ions. Configurations with two K^+ ions in SF1 (9%), and two ions (9%) or four ions (12%) in SF2 were also observed. In contrast, in the simulation with Ca^{2+} ions, no ion reached the binding region SF1. Instead, the outer region SF2 was mostly occupied by two ions (97%). A similar situation was observed in simulations without restraints on the inner and outer helices (Figure S2), which supports the hypothesis that the restraints adopted to prevent the closure of the intracellular gate have marginal effects on the ion binding properties of the SF. The energy maps and the ion occupancies shown in Figure 1 were calculated considering the data collected from two independent trajectories for each ion configuration. Similar results were obtained when the two trajectories were analyzed separately (Figure S3).

The dynamics of the ions during the simulation for the three systems considered was analyzed in the neighborhood of the protein by identifying those ions that got close to protein residues facing the pore (< 4 Å), and measuring the projection along the channel-axis of their coordinates (Figures S4-S6). For the sake of clarity, the permeation properties of each ion species are described considering a single MD trajectory of 200 ns. The same results were observed in a second set of simulations. The data for this second set of trajectories are included in the Supplementary Material. Three complete permeation events are observed in the simulations with Na^+ and K^+ ions. No permeation events are observed in the simulations with Ca^{2+} which binds to SF2 from the extracellular domain and to SC from the intracellular region; no transitions are observed between those sites either. Subsequently, the dynamical behavior of individual ions was analyzed in detail to gain further insight into any specific characteristics of the permeation events, and it is described next.

Simulations with Na^+

5

Figure 2a shows the position along the permeation pathway of the three Na^+ ions that permeate the pore (Na^+_i, Na^+_{ii} and Na^+_{iii}). The permeation of a Na^+ ion can be rationalized as a four-stage process which involves an initial contact with the channel, followed by migration through three main binding sites, referred here as SC, SF1 and SF2. The number of simultaneous ions observed in sites SC and SF1 is mainly one or none (Figure 1b). Indeed, the entrance of Na^+_{ii} (Figure 2a, blue trace) into SC occurs only after Na^+_i (magenta trace) migrates from SC to SF1. Likewise, the occupation of SC by Na^+_{iii} (red trace) only happens after Na^+_{ii} moves to SF1. The number of simultaneous Na^+ ions in SF2 can be up to four, suggesting that release of a given ion from this site (or the entrance in the reversed direction of the ionic current) can occur in the presence of other ions.

To understand the pattern of interactions that gives rise to these permeation events, the distances of all residues close to a given ion during the 200-ns simulation time was analyzed (Figure 2b-d). For the three Na^+ ions, the beginning of the permeation process starts with transient contacts (maximum of ~2 ns) involving residue E684, and with contributions of G683 and V686 from the adjacent chain. This initial contact is followed by the entrance to the SC region, after passing the boundary imposed by I679. During this period, which spans resident times on the order of tens of nanoseconds (Na^+_i ~ 30 ns, Na^+_{ii} ~15 ns, Na^+_{iii} ~ 30 ns), the ion contacts involve primarily residues N676 and Y671, with interaction times ranging from tens of picoseconds up to one nanosecond, approximately. These transient periods indicate that SC does not offer a strong binding site for Na^+ ions.

The next step in the permeation process is the migration from SC to SF1, which is a binding site defined by the carbonyl oxygen atoms of residues G643. Ions remain in this site for times ranging from several hundreds of picoseconds (Na^+_i: Figure 2a, magenta trace and Figure 2b) to over 25 ns (Na^+_{iii}: Figure 2a, red trace and Figure 2d). The final step occurs when the Na^+ ion moves from SF1 to SF2, before being finally released at the other side of the membrane. SF2 offers multiple pinning sites for Na^+ ions, which are defined by the backbone oxygen atoms of M644 and G645, and the carboxylate oxygen atoms of D646 and E648. Once out of the pore, other interacting sites are observed including E600 and D654 at the extracellular region, and E570 at the intracellular region (Figure S7). Such residues are located more than 20 Å away from the permeation pathway, and consequently, they are not likely to be directly involved in the permeation process.

To complement the description of the environment of Na^+ ions moving across the channel, the coordination number and the contributors to the first coordination shell of the cations were assessed (Figure S8a-c). Four levels of dehydration are observed while the ion travels from the intracellular solution through the protein and to the extracellular milieu, corresponding to the loss of one, two, three and four water molecules. Nevertheless, the total number of oxygen atoms in the first coordination shell of the ion remains constant when considering the oxygen atoms contributed by the protein. After migrating from SC to SF1, one or two water molecules are substituted by carbonyl oxygen atoms from residues G643. An example of this situation can be observed for Na^+_{ii} (Figures 2c and

6

S8b) which jumps between the G643 carbonyl oxygen atoms of the four channel subunits following the sequence I → IV → II → IV → II/III → IV → II → IV → II, where protein chains are labeled from I to IV, and being I/III and II/IV opposite to each other. A similar pattern was observed for the other permeating Na$^+$ ions. According to this, when a Na$^+$ ion is in SF1, it resides generally close to the 'wall' of the pore, rather than at its center. However, configurations with ions aligned with the pore axis are also possible, as observed in simulations of Na$^+$ selective channels [16, 24]. This picture is consistent with the observation of two energy minima in SF1, localized at ~1.5 Å from the pore axis, and close to the axis of the pore (energy map in Figure 1b, and occupation densities in Figure S9a-b). To characterize the energy minimum centered on the channel axis, the position of Na$^+_{iii}$ in the x-y plane, orthogonal to the permeation axis, was tracked (Figure S10a). Several short time windows (<1 ns) between 114-123 ns are observed, where both x and y coordinates are close to zero. During these periods, a fully hydrated first shell is only altered by transient contacts with G643 oxygen atoms (Figure S10b-c). When the ion is localized in SF2, residues M644, G645 and D646 dominate the interactions, and desolvation levels of up to four water molecules are detected. For example, Na^+_i loses three water molecules in its first solvation shell when interacting simultaneously with M644, G645 and D646 at ~55 ns, whereas it loses up to four water molecules when it interacts with D645, L647 and E648 at ~80 ns (Figure S8a). At this stage, the interactions with the channel occur in general with one chain at a time (Figure 2b-d). Compared to SF1, there is a similar effect on the position of the ions, as they are mainly localized close to the 'wall' of the pore. This is confirmed by the minimum between G645 and D646 in the free energy landscape (Figure 1b), and the corresponding occupation density map (Figure S9a-b).

The ions previously analyzed correspond to those that effectively diffuse across the channel. However, several other ions interact strongly, for tens of nanoseconds, with the channel at SF1 and SF2 during the simulation (Figure S4). To evaluate the effect of such binding on the conformation of the pore, the RMSD in the region of SF1 and SF2 was measured (Figure 3a). The main observation is a conformational change taking place at ~140 ns. Snapshots of the SF for six conformations during the simulation (one every 40 ns) are shown in Figure 3b. While the relative positions of chains I and IV remain close to their initial configuration, chains II and III come close to each other, which in turn increases the distance between III and IV and decrease the distance between chains II and IV (see black arrows indicating the direction of motion).

The conformational changes of the SF are correlated with the position of the ions close to the pore. Indeed, two ions are localized in between opposite pairs of chains, interacting mainly with D646, and clamping the conformation of SF2 in an arrangement where two opposite pairs of chains are close to each other, while the remaining two pairs are more distant (Figure 3c). The stabilization of the I-IV distance at the experimental value correlates with the binding of one Na$^+$ ion to D646 in chains I and IV (~100 ns), as shown by the black arrow in Figure 3d (the distance of such ion to the protein residues is shown in Figure S11a). Another cation binds initially to D646 of chain III at

7

approximately 110 ns, and it is then coordinated first by D646 of chain II, and subsequently by the carbonyl oxygen atom of L647 of the same chain (Figure S11b). The accomplishment of the dual binding occurs just before 150 ns, when the II-III distance decreases to a value close to the experimental one. These events are summarized in Figure 3d where the relative motions of chains and ions are shown. The same picture of ion permeation emerged from a second MD trajectory of 400 ns. Results for this second simulation are included as Supplementary Material (Figure S12 corresponds to Figure 2, Figure S13 to Figure 3, and Figure S18 to Figure S8). Remarkably, the same structural changes of the SF were observed in this second simulation, with Na^+ ions binding between adjacent chains in SF2 and clamping together these chains (Figure S13c-d).

Simulations with Ca^{2+}

To gain insight into the dynamics of Ca^{2+} ions interacting with the pore channel, three examples were selected among the binding events detected during the simulation and summarized in Figure S5. These events correspond to the binding of two Ca^{2+} ions (Ca^{2+}_i and Ca^{2+}_{ii}) in SF2 (Figure 4a, blue and cyan traces) and a third Ca^{2+} (Ca^{2+}_{iii}) in SC (Figure 4a, red trace). Ions in SF2 were stable, while the ion in SC exhibited a much higher mobility. A Cl^- ion (magenta trace) also entered SC, and remained at this site for almost 100 ns. The distances between the Ca^{2+} ions and the center of mass of the oxygen atoms of the residues of the pore are shown in Figures 4b-d. These profiles show that Ca^{2+}_i and Ca^{2+}_{ii} are coordinated by the carboxylate groups of two D646 residues from adjacent chains. Additional weaker interactions (distance >4 Å) are observed with the backbone oxygen atoms of M644 and G645. In the case of Ca^{2+}_{iii}, localized at SC, the pattern of contacts shows that only transient contacts with N676 and Y671 are formed. This is in agreement with the desolvation pattern occurring upon binding (Figure S8d-e). In the case of Ca^{2+}_i, two water molecules from the coordination shell are lost when the ion binds to D646 from chain II, followed by a further reduction of two water molecules when D646 from chain III interacts with Ca^{2+}_i. The total number of coordinated oxygen atoms from water and protein remains constant in the first coordination shell. In the case of Ca^{2+}_{iii}, a reduction of two water molecules occurs in the time window between ~55-155 ns with no compensation by the protein oxygen atoms (black and red lines superimpose almost perfectly). This time window coincides with the period when a Cl^- ion is localized in SC, altering the solvation of the Ca^{2+} ion. Figure S9c shows the structure of the permeation pathway along with occupation iso-surfaces of the three Ca^{2+} ions, providing a structural picture of the localization of the ions in the pore.

The stability of Ca^{2+} binding at SF2 raises questions about the specific structure of the SF region, also considering the structural effect that Na^+ binding has in the SF. To account for this, the RMSD of the backbone atoms of the SF residues G643 to E648 was calculated (Figure 5a). The general trend observed is seemingly a conformational change after ~110 ns, with RMSD value changing from 1.5 Å to 1.9 Å. An illustration of such changes is depicted in Figures 5b and 5d, where the protein structure and the position of ions Ca^{2+}_i and Ca^{2+}_{ii} are shown superimposed in

8

six frames from the simulation (one every 40 ns). Ca^{2+}_i, which initially interacts only with D646 of chain II, at ~110 ns moves toward residue D646 of chain III, forming a double salt-bridge (notably in the same manner that Ca^{2+}_{ii} does), which is stable for the remaining of the simulation (Figure 4b-d). At the same time the distance between chains II and III decreases to the same value observed for chains I and IV, which are also linked by a Ca^{2+} ion (Ca^{2+}_{ii}). This indicates that such binding could stabilize the conformation adopted by the SF with pairs of adjacent chains clamped together by a Ca^{2+} ion. Identical results were observed in a second MD trajectory of 400 ns (Figure S14 corresponds to Figure 4, Figure S15 to Figure 5, and Figure S18 to Figure S8).

Simulations with K^+

The same analysis presented for Na^+ and Ca^{2+} ions in the previous sections will be described for K^+ in what follows in order to have a complete computational description of the most biologically relevant cations. Although during the simulation it was observed that many K^+ ions interact with the conduction pore, only one ion (K^+_i) is actually able to permeate the channel, another ion occupies extensively site SC (K^+_{ii}), and several other ions briefly interact with the SF domain (Figure 6 and S6). These observations are illustrated in the occupation density maps of K^+_i and K^+_{ii} which provide a tridimensional picture of the localization of the ions during the permeation process (Figure S9d). The trajectory of the permeating ion is similar to the ones observed for Na^+ ions (Figure 6a). The main difference is that K^+_i enters straightaway in SC, without any prior contact with any residue. Once inside the cavity, K^+_i interacts weakly with residues N676 and Y671, like it was also observed for both Na^+ and Ca^{2+}. Before migrating to SF1/SF2, two returning events are observed where transient interactions with G643 induce jumps between SC and SF1. In the latest of those jumps, K^+_i migrates to SF2 where it stays for a brief period of time (~4 ns), and subsequently escapes to the other side of the membrane.

Isolated desolvation events are observed in SC for K^+ ions. These events correspond to one water molecule of the first solvation shell being substituted by the carbonyl oxygen atom of N676 or by the hydroxyl oxygen of Y671 (Figures S8f-g). While in SF1, the ion shows desolvation levels of one and two water molecules from the first solvation shell, corresponding to single and double simultaneous coordination of K^+_i by the carbonyl oxygen atom of G643 from different chains. It is worth noting that in the final SF1 binding event, a triple coordination of K^+_i by G643 is observed which is able to induce desolvation of three water molecules, an event that was never observed for Na^+ ions. To further confirm this behavior, the total number of oxygen atoms contributed by protein residues to the ion coordination shell was computed for all the ions in each binding site (Figure 7). In agreement with the previous observation, while a Na^+ ion is coordinated by one or two oxygen atoms in SF1, K^+ frequently reaches values of two and three, and although significantly less frequently, events where all four chains come together to make contact with a single K^+ in SF1 are possible.

To complete the analysis, changes in the structure of the SF and the potential effects on its conformation by the

9

binding of ions were analyzed. In Figure 8a, the RMSD of the SF is presented; fluctuations are observed around ~1.6 Å from the experimental structure without net conformational changes. Figure 8b shows six superimposed structures of the SF taken every 40 ns, in order to describe the conformational sampling of such fluctuations. In accordance with the RMSD values, no clear relative motions of the chains are observed. In contrast, the chains fluctuate around positions close to the initial conformation. This is significantly different to what it was described for Na^+ and Ca^{2+} ions, where relative chain displacements were observed, leading to conformations that consisted of a dimer of dimers (I-IV and II-III) with inter-chain distances either similar or greater than the experimental value (Figures 3c and 5c). Instead, in the presence of K^+ ions, the four chains fluctuate collectively, without any noticeable asymmetric behavior (Figure 8c).

Considering that an asymmetric behavior appears to be enhanced by the binding of Na^+ and Ca^{2+} ions to SF2, it is also worth analyzing the binding of K^+ ions in order to identify any relevant differences. Figure 8d illustrates that K^+ ions are uniformly distributed in SF2, contrary to the picture for Na^+ and Ca^{2+}, where two ions are coordinated by pairs of adjacent chains (Figures 3d and 5d). A more stringent test for such observation is the calculation of the pattern of ion interactions close to SF2. When considering the Na^+ and Ca^{2+} systems, two ions strongly interact with two chain pairs (I-IV and II-III) simultaneously, and a specific conformation of SF2 is observed. In contrast, only one K^+ ion engages in an interaction with a chain pair in the SF2 site (I-IV) for approximately 40 ns (Figure S11c). This time scale appears insufficient to induce the conformational changes observed in the case of the other two cations. Moreover, such structural change observed for Na^+ and Ca^{2+} seems to require the binding of two ions to SF2 instead of only one, as observed for K^+. However, it is worth noting that when K^+ establishes a dual interaction, the distance between the corresponding chains is close to the experimental value (Figure 8c, ~50 ns blue trace). A second MD trajectory of 200 ns provided similar results (Figure S16 corresponds to Figure 6, Figure S17 to Figure 8, and Figure S18 to Figure S8). Since the structure of the filter in simulations with K+ ions did not exhibit any net structural change, but only thermal oscillations, the total simulated time was lower for K^+ compared to Na^+ and Ca^{2+} (400 ns versus 600 ns).

Discussion

The experimental tridimensional structure of TRPV1 is of the utmost importance for improving our current understanding of ion channels belonging to the Transient Receptor Potential family. In order to understand how ion conduction takes place at the atomic level, it is necessary to complement the experimental structural data with dynamical information, a description of the ion binding sites and of the permeation pathway. The MD simulations presented in this study reveal the presence of three main binding sites for cations along the pore of TRPV1, one corresponding to the intracellular cavity of the channel, and the other two to the intracellular and extracellular entrances of the SF. The binding site in the intracellular cavity is similar to the analogous site observed in other ion

10

channels, for instance K^+ channels [25] , Na^+ channels [26], or the NaK channel [27]. Despite the gating mechanism of TRPV1 seems slightly different from that of voltage-gated channels, in both cases, the intracellular cavity corresponds to a wide attractive region where cations are free to diffuse. This is a consequence of the conserved architecture among diverse ion channels, which makes the intracellular cavity continuous with the cytoplasm, reducing the actual permeation pathway to the sole SF.

The outer entrance of the SF exerts an electrostatic attraction on cations due to the presence of two rings of acidic residues formed by E648, and D646 close to the permeation pathway. While the presence of binding sites for cations in this region was largely expected, the MD trajectories revealed some unpredictable effects of ion binding on the structure of the SF. Potassium ions diffuse easily in this region, with binding events of K^+ ions to D646 lasting from a few picoseconds to up to 10 ns, with only one exception of a ~40 ns long binding event. Instead, several binding events of Na^+ ions to D646 with residence times above 100 ns were sampled. The different behavior observed between Na^+ and K^+ ions might be a consequence of the difference in size, which stabilizes Na^+ binding to high-field-strength sites, like the side chain of glutamate residues [28]. The stable binding of Na^+ ions to residue D646 is correlated with a structural change of the SF. Na^+ ions act as bridges between adjacent chains of the SF, linking together D646 residues from two adjacent chains. This conformation of the SF can be described as a dimer of dimers, as opposed to a symmetric homo-tetramer. An asymmetric structure of the SF is in sharp contrast to the symmetric structure observed experimentally, a property that was instead preserved in simulations with K^+ ions. Therefore, the simulations suggest that the structure of the SF changes in response to the permeating ions.

Permeation of Na^+ and K^+ ions entails the presence of a third binding site at the inner entrance of the SF. In the case of K^+ ions, this intracellular binding site is similar to the analogous region in Na^+ selective channels, namely a large site (diameter ~8 Å) surrounded by carbonyl oxygen atoms, with a symmetric architecture. Instead, in the presence of Na^+ ions, the symmetry of the SF is broken also at its intracellular entrance. However, this does not prevent the binding of ions to this region, and rapid transitions to/from the intracellular cavity or the extracellular side of the SF. The situation is completely different in simulations with Ca^{2+} ions. We did not observe any Ca^{2+} ion reaching the intracellular entrance of the SF. There are several possible reasons for this, which are not mutually exclusive. Firstly, transitions of Ca^{2+} ions to this region might be lacking because the simulated trajectories are not long enough. However, numerous binding events of K^+ and Na^+ ions in this region were sampled during identical simulation time, which makes this explanation unlikely. An alternative hypothesis is that Ca^{2+} ions are poorly described in the model adopted for the simulations [29]. In particular, in the case of divalent Ca^{2+} ions, the absence of polarization effects in the adopted force field might result in simulation artifacts [30–32]. However, non-polarizable force fields were able to describe permeation of Ca^{2+} ions in bacterial Na^+ channels [33, 34]. Calcium ions entered the SF of Na^+-channels, reaching the intracellular entrance, in simulations of comparable length of the ones presented here. The filter of Na^+-

11

channels and TRPV1 are similar, with an intracellular entrance lined by carbonyl oxygen atoms, and an extracellular entrance surrounded by acidic residues [35]. Therefore, it is unlikely that inaccuracies of the force fields prevent the passage of Ca^{2+} ions through the calcium selective TRPV1 channel, and not in a Na^+ selective one. A final hypothesis to explain the lack of permeation in the simulations with Ca^{2+} ions is that this is a consequence of the TRPV1 structure and its dynamics. The transition to an asymmetric structure observed in the simulations with Na^+ ions, is even more extreme in simulations with Ca^{2+} ions. An ion approaching the SF from the intracellular cavity gets into contact with a highly asymmetric binding site, with a minimum distance between opposite side chains close to 7 Å. At the same time, on the extracellular side, the entrance of the SF is lined by two Ca^{2+} ions, which are stably bound to residues D646. The distance between these Ca^{2+} ions is ~7 Å, while the analogous Na^+ ions are ~12 Å apart. This might explain why Na^+ ions were able to reach the intracellular side of the SF, while this transition was forbidden for Ca^{2+} ions. This hypothesis implies that the structure of the SF of TRPV1 permeable to Ca^{2+} ions is not the one observed experimentally, nor the one sampled in our MD trajectories. In other words, a structural change has to take place in the SF to increase its permeability to Ca^{2+}, and this transition is still missing in our simulations. Transitions of TRPV1 between states with different ion selectivity were already observed experimentally [8].

In summary, the simulations presented in this study reveal a unique feature of the TRPV1 channel, the high flexibility of its SF. The channel was permeable to Na^+ and K^+ ions, but the structure of the SF was different in these two cases. In addition, permeation events were not observed for Ca^{2+} ions, and this led to the hypothesis that further conformational changes of the SF are required to allow Ca^{2+} permeability. The lack of hydrogen bonds between the residues of the loop helices at the back of the SF is likely to be responsible for the higher mobility of TRPV1 compared to the other ion channels [3, 35, 36]. The conductive conformation of the SF of other ion channels known to date is characterized by a unique tridimensional structure [3, 35, 36]. This is true for K^+ selective channels, where the only known transition of the SF results in channel inactivation [37, 38], as well as for Na^+ selective channels [39]. In this respect, the highly flexibility of the SF of TRPV1 seems to cast this channel apart, and the MD trajectories presented in this study provide a first glimpse of this process at the atomic level.

Materials and Methods

Model Definitions

The initial atomic model was based on the structure of the TRPV1 channel determined by electron microscopy at a resolution of 3.80 Å (Protein data bank entry 3J5Q). Only the pore domain was considered in the model (residue 570 to 686). The N-terminus was acetylated and an N-methylamide group was added to the C-terminus. Default ionization states were used for the remaining amino acids. The channel was embedded in a pre-equilibrated lipid bilayer of 256 1-Palmitoyl,2-oleoyl-sn-Glycero-3-phosphocholine (POPC) molecules, with the axis aligned to the

12

bilayer normal, and the extracellular aromatic belt (amino acids F655) aligned to the bilayer surface. Lipid molecules closer than 1.0 Å to protein atoms were removed. The atomic system was solvated by the *Solvate* plug-in of VMD [40], and then water molecules within 1.2 Å of protein and lipid atoms were removed. Ions were added to the system to obtain a total ionic concentration of 150 mM.

Molecular Dynamics Simulations

Dynamics of variable length were performed using version 2.9 of NAMD [41, 42]. The CHARMM force field with CMAP correction [43, 44] was used for lipid, ions and protein, together with TIP3P model for water molecules [45]. The particle mesh Ewald algorithm was used to treat the electrostatics interactions [46]. Van der Waals forces were smoothly switched off at 10-12 Å. Bonds with hydrogen atoms were restrained by the SETTLE algorithm [47], in order to use a 2 fs time step. The multi time step algorithm r-RESPA [48] was used to integrate the equation of motion. Non-bonded short-range forces were computed every time step, while electrostatic forces were updated every 2 time steps. MD simulations were performed in the NpT ensemble. Pressure was kept at 1 atm by the Nose-Hoover Langevin piston method [49, 50], with a damping time constant of 100 ps and a period of 200 ps. Temperature was kept at 303 K by coupling to a Langevin thermostat, with a damping coefficient of 5 ps^{-1}. The systems were equilibrated using 10,000 steps of energy minimization with harmonic restraints on the protein heavy atoms (force constant equal to 10 kcal mol^{-1} $Å^{-2}$). Harmonic restraints were gradually reduced to zero in the course of a 4 ns equilibration trajectory. Afterwards, independent trajectories were simulated for each system: (i) a 200 ns trajectory with no restraints applied; (ii) and two sets of trajectories (two sets of 200 ns in the presence of 150 KCl, 200 ns and 400 ns in the presence of 150 mM NaCl or $CaCl_2$) with harmonic restraints applied to the Cα atoms of the intracellular terminal of helices S5 and S6 (residues 570 to 577 and 679 to 688) with a force constant of 1 kcal mol^{-1} $Å^{-2}$.

13

FIGURE CAPTIONS

Figure 1. (a) Structure of the TRPV1 channel with residues 679, 671, and 641 to 646 in licorice representation. Energy maps for Na^+ (b), Ca^{2+} (c), and K^+ (d) ions. Energies were calculated from the probability histograms of the ions positions in the MD trajectories over a 2-dimensional space defined by: the distance along the z-axis between the ion and the carbonyl oxygen atoms of residues G643; and the distance in the x-y plane between the ion and the center of the carbonyl oxygen atoms of residues G643 (r-axis). The data to calculate the probability histograms were gathered from two independent simulations for each ion type (200 and 400 ns for Na^+ and Ca^{2+}; two of 200 ns for K^+). The radial and axial direction were discretized in bins with both sides equal to 0.5 Å. The dotted lines show the average position of the center of the carbonyl oxygen atoms of residues I679, G643, G645 (carbonyl oxygen atoms of Met644 are at the same z-value of G645); of the hydroxyl oxygen atoms of residues Y671; and of the carboxylic oxygen atoms of residues D646 and E648. The probability histograms on the right side of the energy maps shows the number of ions between the centers of the carboxylic groups of residues D646 and the carbonyl oxygen atoms of residues M644 (upper plot in each panel, binding region SF2); between the centers of the carbonyl oxygen atoms of residues M644 and the hydroxyl oxygen atoms of residues Y671 (middle plot, binding regions SF1), and between the hydroxyl oxygen atoms of residues Y671 and the carbonyl oxygen atoms of residues I679 (lower plot, binding region SC). The y-axis of the probability histograms extends from 0 to 1.

Figure 2. Permeation of Na^+ across TRPV1 pore. (a) Projection on the z-axis of the position of the geometric center of relevant oxygen atoms (I679-O, Y671-OH, G643-O, M644-O, D646-OD1/2 and E648-OE1/2) from the permeation pathway (black traces), and permeating ions (Na^+_i: magenta, Na^+_{ii}: blue, Na^+_{iii}: red) taken from Figure S3. A schematic picture of the binding sites of the ions in the permeation pathway is shown on the right. **(b-d)** Distance between Na^+_i, Na^+_{ii} and Na^+_{iii} and the center of mass of the closest oxygen atoms from the protein residues during their permeation. Periods of binding to a specific site during permeation is delimited by vertical dotted lines.

Figure 3. Filter domain dynamics in the presence of Na^+. (a) RMSD of the SF backbone (residues 643 to 648). **(b)** Distance between adjacent subunits measured using the Cα atoms of residue D646 from chain pairs I-II (black), II-III (red), III-IV (magenta) and IV-I (blue). The black dotted line indicates the corresponding experimental value (PDBID: 3J5Q). **(c)** Superposition of six conformations of the SF (residues 643 to 648) taken every 40 ns from a 200 ns simulation, colored by time-step (from red to blue: beginning to end of the simulation). The black arrows indicate relative motions of the filter subunits. **(d)** As in (c) but adding the Na^+ ions close to SF2 in each conformation.

Figure 4. Permeation of Ca^{2+} across TRPV1 pore. (a). Projection on the z-axis of the position of the center of mass of relevant oxygen atoms (I679-O, Y671-OH, G643-O, M644-O, D646-OD1/2 and E648-OE1/2) from the permeation path (black traces) and the ions that bind stably to the channel (blue: Ca^{2+}_i, cyan: Ca^{2+}_{ii}, red: Ca^{2+}_{iii},

14

magenta: Cl⁻), taken from Figure S4. A schematic picture of the binding sites of the ions in the permeation pathway is shown on the right. **(b-d).** Distance between Ca^{2+}_i, Ca^{2+}_{ii} and Ca^{2+}_{iii} and the center of mass of the closest oxygen atoms from the protein residues. Periods of binding to a specific site during permeation is delimited by vertical dotted lines.

Figure 5. Filter domain dynamics in presence of Ca^{2+}. As Figure 3 but for Ca^{2+} ions.

Figure 6. Permeation of K^+ across TRPV1 pore. (a). Projection on the z-axis of the position of the center of mass of relevant oxygen atoms (I679-O, Y671-OH, G643-O, M644-O, D646-OD1/2 and E648-OE1/2) in the permeation path (black traces) and the ions that permeate or bind to the channel (blue: K^+_i: blue: K^+_{ii}:red), selected from Figure S6. A schematic picture of the binding sites of the ions in the permeation pathway is shown on the right. **(b-d).** Distance between ions K^+_i and K^+_{ii} and the center of mass of the closest oxygen atoms from the protein residues. Periods of binding to a specific site during permeation is delimited by vertical dotted lines.

Figure 7. Coordination number of ions in the SF. Coordination number of Na^+ (left), K^+ (middle) and Ca^{2+} (right), as a function of the position along the permeation pathway. The data was taken from 2 independent simulations for each ion type (200 and 400 ns for Na^+ and Ca^{2+}; and two 200 ns for K^+). A schematic representation is shown on the far left to facilitate the localization of SF1 and SF2.

Figure 8. Filter domain dynamics in presence of K^+. As Figure 3 but for K^+ ions.

References

[1]   Venkatachalam K, Montell C. TRP Channels. Annu Rev Biochem 2007;76:387–417.

[2]   Nilius B, Owsianik G. Transient receptor potential channelopathies. Pflüg Arch - Eur J Physiol 2010;460:437–50.

[3]   Liao M, Cao E, Julius D, Cheng Y. Structure of the TRPV1 ion channel determined by electron cryo-microscopy. Nature 2013;504:107–12.

[4]   Julius D. TRP Channels and Pain. Annu Rev Cell Dev Biol 2013;29:355–84.

[5]   Caterina MJ, Schumacher MA, Tominaga M, Rosen TA, Levine JD, Julius D. The capsaicin receptor: a heat-activated ion channel in the pain pathway. Nature 1997;389:816–24.

[6]   Ramsey IS, Delling M, Clapham DE. An introduction to TRP channels. Annu Rev Physiol 2006;68:619–47.

[7]   Lishko PV, Procko E, Jin X, Phelps CB, Gaudet R. The Ankyrin Repeats of TRPV1 Bind Multiple Ligands and Modulate Channel Sensitivity. Neuron 2007;54:905–18.

[8]   Chung M-K, Güler AD, Caterina MJ. TRPV1 shows dynamic ionic selectivity during agonist stimulation. Nat Neurosci 2008;11:555–64.

[9]   Owsianik G, Talavera K, Voets T, Nilius B. Permeation and selectivity of TRP channels. Annu Rev Physiol 2006;68:685–717.

[10] Domene C, Vemparala S, Furini S, Sharp K, Klein ML. The role of conformation in ion permeation in a K^+ channel. J Am Chem Soc 2008;130:3389–98.

[11] Domene C, Furini S. Dynamics, Energetics, and Selectivity of the Low-K^+ KcsA Channel Structure. J Mol Biol 2009;389:637–45.

[12] Furini S, Domene C. Selectivity and Permeation of Alkali Metal Ions in K^+-channels. J Mol Biol 2011;409:867–78.

[13] Furini S, Domene C. Nonselective Conduction in a Mutated NaK Channel with Three Cation-Binding Sites. Biophys J 2012;103:2106–14.

[14] Furini S, Domene C. K^+ and Na^+ Conduction in selective and nonselective ion channels via molecular dynamics simulations. Biophys J 2013;105:1737–45.

[15] Furini S, Domene C. Atypical mechanism of conduction in potassium channels. Proc Natl Acad Sci 2009;106:16074–7.

[16] Furini S, Domene C. On conduction in a bacterial sodium channel. PLoS Comput Biol 2012;8:e1002476.

[17] Bernèche S, Roux B. Energetics of ion conduction through the K^+ channel. Nature, 2001, 414, 6859; 73-77.

[18] Aqvist J, Luzhkov V. Ion permeation mechanism of the potassium channel. Nature, 2000, 404, 6780, 881-884.

[19] Corry B, Thomas M. Mechanism of ion permeation and selectivity in a voltage gated sodium channel. J. Am

Chem Soc 2012, 134 (3), 1840-6.

[20] Boiteux C, Vorobyov I, Allen TW. Ion conduction and conformational flexibility of a bacterial voltage-gated sodium channel. Proc Natl Acad Sci 2014, 111 (9) 3454-3459.

[21] Chakrabarti N, Ing C, Payandeh J, Zheng N, Catterall WA, Pomès R. Catalusis of Na^{+} permeation in the bacterial sodium channel Na(V)Ab. Proc Natl Acad Sci U S A. 2013 110(28), 11331-6

[22] Jensen MO, Borhani DW, Lindorff-Larsen K, Maragakis P, Jogini V, Eastwood MP, et al. Principles of conduction and hydrophobic gating in K^{+} channels. Proc Natl Acad Sci 2010, 107, 5833–8.

[23] Hui K, Liu B, Qin F. Capsaicin activation of the pain receptor, VR1: multiple open states from both partial and full binding. Biophys J 2003, 84, 2957–68.

[24] Stock L, Delemotte L, Carnevale V, Treptow W, Klein ML. Conduction in a Biological Sodium Selective Channel. J Phys Chem B 2013, 117, 3782–9.

[25] Doyle DA, Morais Cabral J, Pfuetzner RA, Kuo A, Gulbis JM, Cohen SL, Chait BT, MacKinnon R. The structure of the potassium channel: molecular basis of K^{+} conduction and selectivity. *Science* 1998, **280**, 69–77.

[26] Payandeh J, Gamal El-Din TM, Scheuer T, Zheng N, Catterall WA. Crystal structure of a voltage-gated sodium channel in two potentially inactivated states. Nature 2012, **486**, 135–139.

[27] Alam A, Jiang Y. Structural analysis of ion selectivity in the NaK channel. Nat Struct Mol Biol 2009, 16, 35–41.

[28] Eisenman G, Horn R. Ionic selectivity revisited: the role of kinetic and equilibrium processes in ion permeation through channels. J Membr Biol 1983, 76, 197–225.

[29] Illingworth CJ, Domene C. Many-body effects and simulations of potassium channels. Proc R Soc Math Phys Eng Sci 2009, 465, 1701–16.

[30] Illingworth CJR, Furini S, Domene C. Computational Studies on Polarization Effects and Selectivity in K^{+} Channels. J Chem Theory Comput 2010, 6, 3780–92.

[31] Allen TW, Andersen OS, Roux B. Ion permeation through a narrow channel: using gramicidin to ascertain all-atom molecular dynamics potential of mean force methodology and biomolecular force fields. Biophys J 2006, 90, 3447–68.

[32] Warshel A, Kato M, Pisliakov AV. Polarizable force fields: history, test cases, and prospects. J Chem Theory Comput 2007, 3, 2034–45.

[33] Corry B. Na[+]/Ca^{2+} selectivity in the bacterial voltage-gated sodium channel NavAb. PeerJ 2013, 1:e16.

[34] Ke S, Zangerl E-M, Stary-Weinzinger A. Distinct interactions of Na^{+} and Ca^{2+} ions with the selectivity filter of the bacterial sodium channel NaVAb. Biochem Biophys Res Commun 2013, 430,1272–6.

[35] Payandeh J, Scheuer T, Zheng N, Catterall WA. The crystal structure of a voltage-gated sodium channel. Nature 2011;475:353–8.

[36] Doyle DA, Morais Cabral J, Pfuetzner RA, Kuo A, Gulbis JM, Cohen SL, et al. The structure of the potassium channel: molecular basis of K^+ conduction and selectivity. Science 1998, 280, 69–77.

[37] Zhou Y, Morais-Cabral JH, Kaufman A, MacKinnon R. Chemistry of ion coordination and hydration revealed by a K^+ channel-Fab complex at 2.0 A resolution. Nature 2001, 414, 43–8.

[38] Cuello LG, Jogini V, Cortes DM, Perozo E. Structural mechanism of C-type inactivation in K^+ channels. Nature 2010, 466, 203–8.

[39] Payandeh J, Gamal El-Din TM, Scheuer T, Zheng N, Catterall WA. Crystal structure of a voltage-gated sodium channel in two potentially inactivated states. Nature 2012, 486(7401),135-9.

[40] Humphrey W, Dalke A, Schulten K. VMD: Visual molecular dynamics. J Mol Graph 1996, 14, 33–8.

[41] Phillips JC, Braun R, Wang W, Gumbart J, Tajkhorshid E, Villa E, et al. Scalable molecular dynamics with NAMD. J Comput Chem 2005, 26, 1781–802.

[42] Kalé L, Skeel R, Bhandarkar M, Brunner R, Gursoy A, Krawetz N, et al. NAMD2: Greater Scalability for Parallel Molecular Dynamics. J Comput Phys 1999, 151, 283–312.

[43] MacKerell, AD, Bashford D, Bellott M, Dunbrack, RL, Evanseck JD, Field MJ, et al. All-Atom Empirical Potential for Molecular Modeling and Dynamics Studies of Proteins. J Phys Chem B 1998, 102, 3586–616.

[44] Brooks BR, Bruccoleri RE, Olafson BD, States DJ, Swaminathan S, Karplus M. CHARMM: A program for macromolecular energy, minimization, and dynamics calculations. J Comput Chem 1983, 4, 187–217.

[45] Jorgensen WL, Chandrasekhar J, Madura JD, Impey RW, Klein ML. Comparison of simple potential functions for simulating liquid water. J Chem Phys 1983, 79, 926.

[46] Essmann U, Perera L, Berkowitz ML, Darden T, Lee H, Pedersen LG. A smooth particle mesh Ewald method. J Chem Phys 1995, 103, 8577.

[47] Miyamoto S, Kollman PA. Settle: An analytical version of the SHAKE and RATTLE algorithm for rigid water models. J Comput Chem 1992, 13, 952–62.

[48] Tuckerman M, Berne BJ, Martyna GJ. Reversible multiple time scale molecular dynamics. J Chem Phys 1992; 97:1990.

[49] Martyna GJ, Tobias DJ, Klein ML. Constant pressure molecular dynamics algorithms. J Chem Phys 1994, 101, 4177.

[50] Feller SE, Zhang Y, Pastor RW, Brooks BR. Constant pressure molecular dynamics simulation: The Langevin piston method. J Chem Phys 199, 103, 4613.
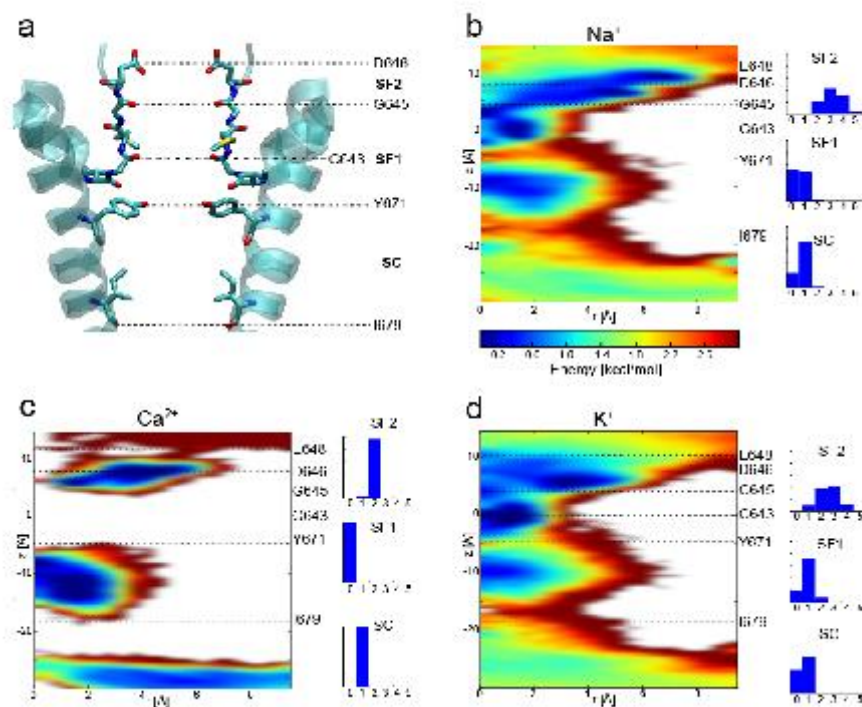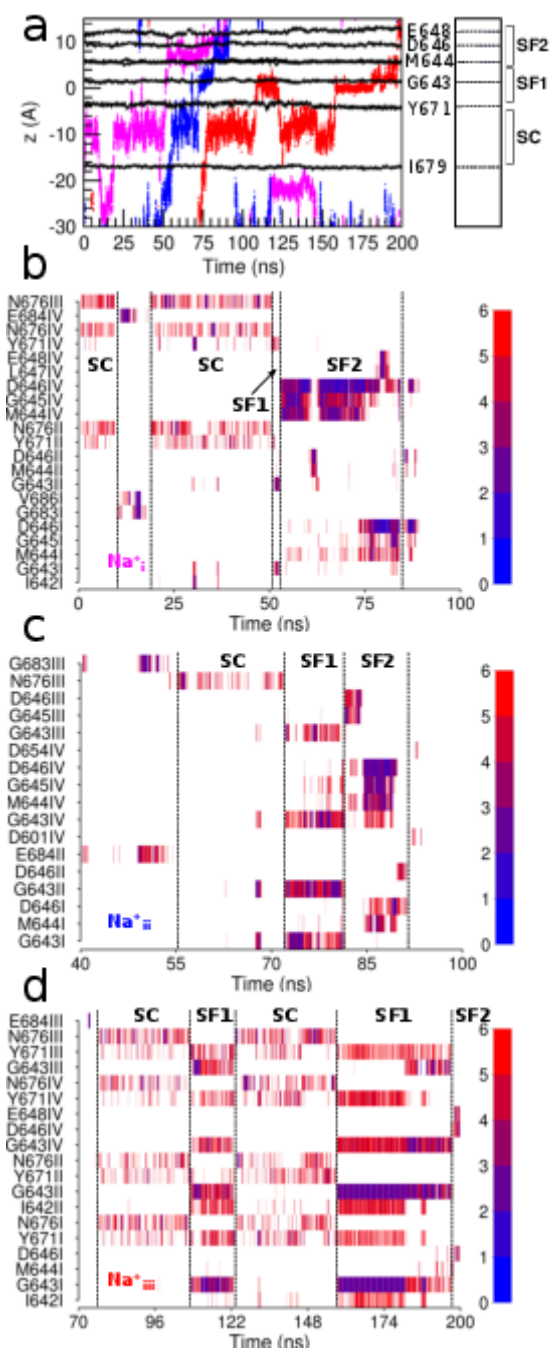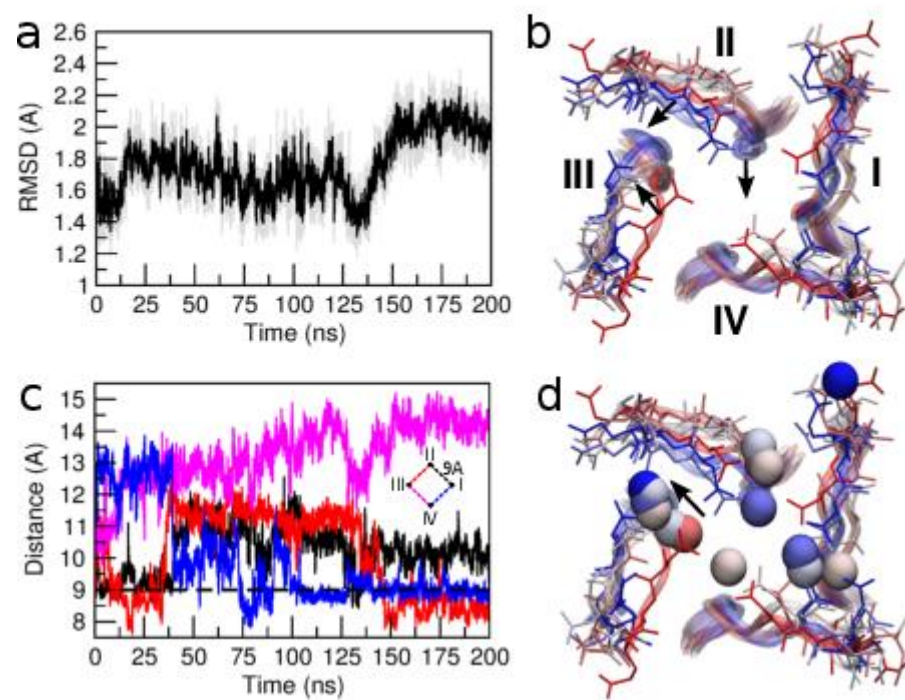
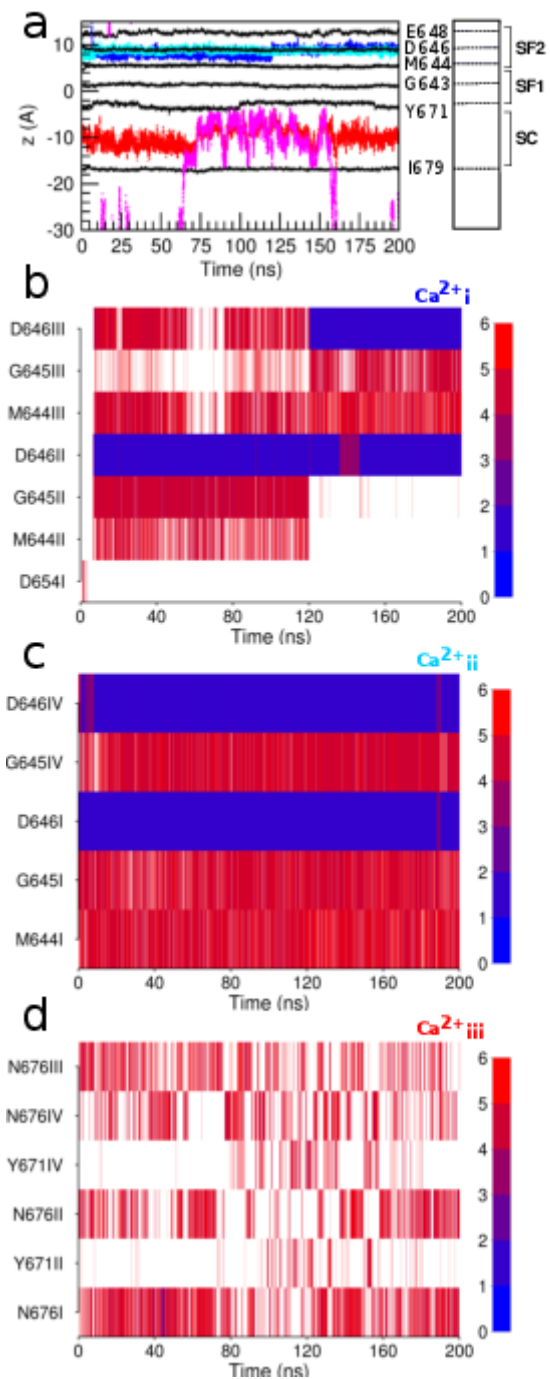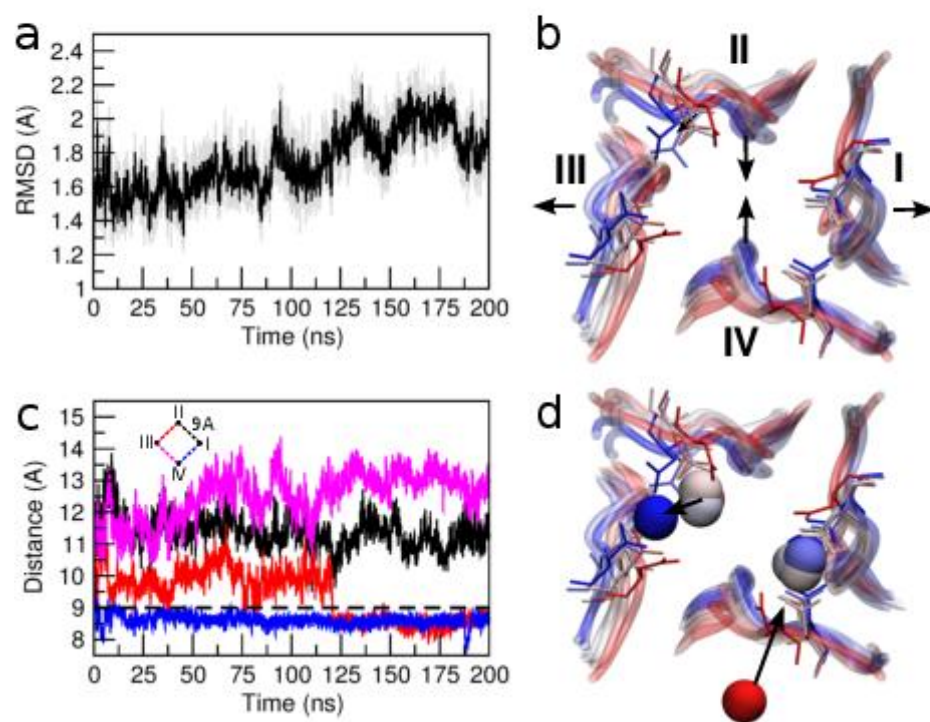Figure 1

19

Figure 2

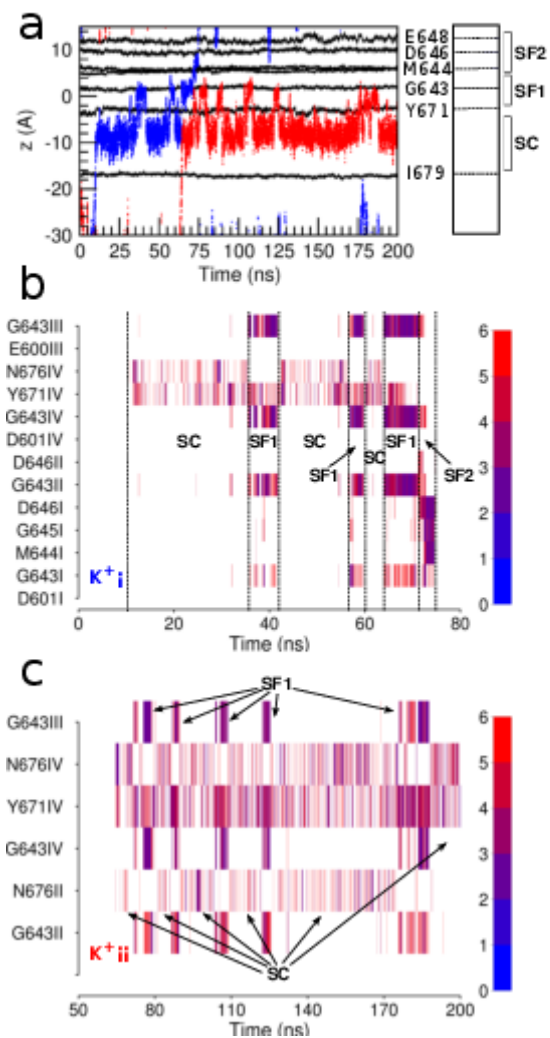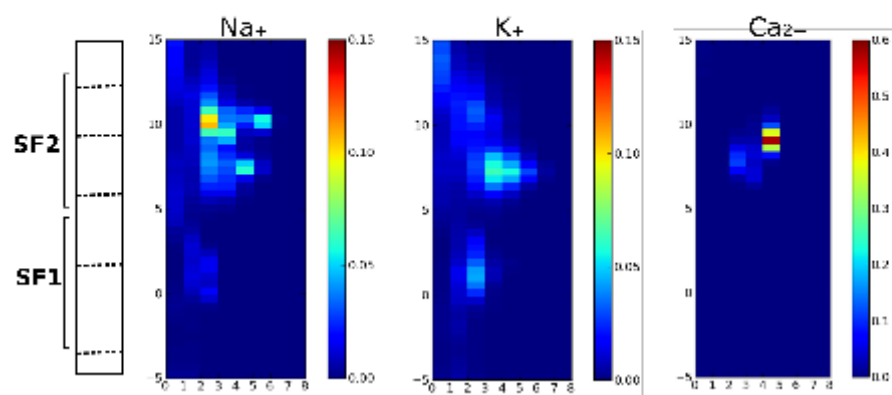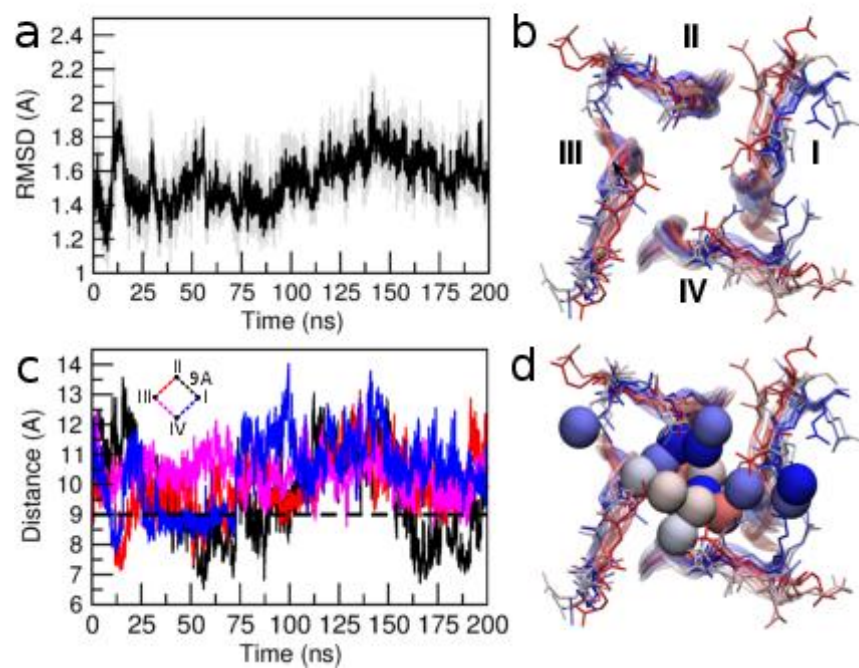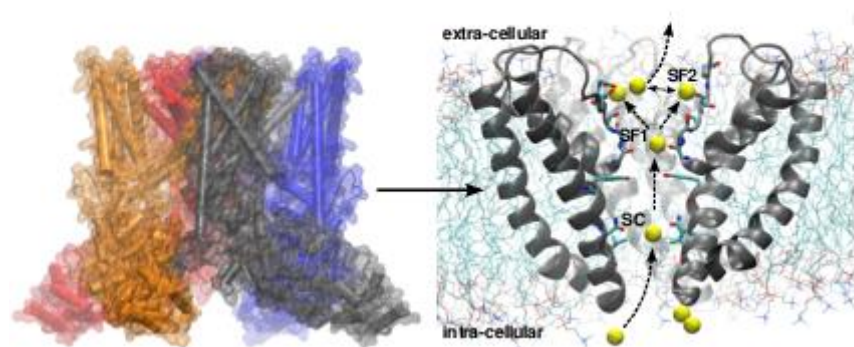Figure 3

Figure 4

22

Figure 5

Figure 6

24

Figure 7

Figure 8

Graphical abstract

Highlights

- Ion conduction in TRPV1 was analyzed by molecular dynamics simulations

- Three main binding sites (SC, SF1 and SF2) define the permeation pathway

- Binding of Na^+ and Ca^{2+} ions (but not K^+) to SF2 links adjacent pore subunits

- The structure of the selectivity filter is sensible to the permeating ionic species

28